FEATURE ARTICLE

The Optical Properties of Metal Nanoparticles: The Influence of Size, Shape, and Dielectric Environment

K. Lance Kelly, Eduardo Coronado, Lin Lin Zhao, and George C. Schatz*

Department of Chemistry, Northwestern University, Evanston, Illinois 60208-3113

Received: August 9, 2002

The optical properties of metal nanoparticles have long been of interest in physical chemistry, starting with Faraday's investigations of colloidal gold in the middle 1800s. More recently, new lithographic techniques as well as improvements to classical wet chemistry methods have made it possible to synthesize noble metal nanoparticles with a wide range of sizes, shapes, and dielectric environments. In this feature article, we describe recent progress in the theory of nanoparticle optical properties, particularly methods for solving Maxwell's equations for light scattering from particles of arbitrary shape in a complex environment. Included is a description of the qualitative features of dipole and quadrupole plasmon resonances for spherical particles; a discussion of analytical and numerical methods for calculating extinction and scattering cross-sections, local fields, and other optical properties for nonspherical particles; and a survey of applications to problems of recent interest involving triangular silver particles and related shapes.

I. Introduction

Gold colloidal nanoparticles are responsible for the brilliant reds seen in stained glass windows. Silver particles are typically yellow. These properties have been of interest for centuries, and scientific research on metal nanoparticles dates at least to Michael Faraday.[1] It was therefore one of the great triumphs of classical physics when in 1908, Mie presented a solution to Maxwell's equations[2−4] that describes the extinction spectra (extinction = scattering + absorption) of spherical particles of arbitrary size. Mie's solution remains of great interest to this day,[5] but the modern generation of metal nanoparticle science, including applications to medical diagnostics[6] and nanooptics,[7] has provided new challenges for theory. In this paper, we highlight recent advances in theoretical research in this area, emphasizing especially the linear optical properties (extinction, absorption, Rayleigh scattering, and Raman scattering) of isolated silver particles of arbitrary shape with sizes up to a few hundred nanometers.

One of the reasons why Mie's theory has remained important for so long is that it is the only simple, exact solution to Maxwell's equations that is relevant to particles. In addition, most of the standard colloidal preparations yield particles that are approximately spherical, and most of the optical methods for characterizing nanoparticle spectra probe a large ensemble of these particles. This leads to results that can be modeled reasonably well using Mie theory. Recently, however, there has been growing interest in characterizing the optical properties of metal nanoparticles that are made using lithographic methods such as nanosphere lithography,[8] e-beam lithography,[9] and other methods,[10,11] which produce well-defined sizes and nonspherical shapes without aggregation. In addition, variations on classical wet chemistry techniques have been developed that give high yields of nonspherical particles, especially rods[12] and triangles.[13] The shapes and sizes of these particles are better characterized than in the past using electron and scanning probe microscopy,

and in some cases, the optical properties of individual nanoparticles have been determined.[14] However, there are often complicating factors in understanding the nanoparticle optical properties, including the presence of a supporting substrate, a solvent layer on top of the particles, and particles that are close enough together that their electromagnetic coupling changes the spectra. All of these factors motivate the need for theory that can describe the electrodynamics of nanoparticles of arbitrary shape and size subject to a complex external dielectric environment.[15−21] Although extinction, absorption, and scattering are still the primary optical properties of interest, other spectroscopic techniques are also being brought to bear on these particles, including surface-enhanced Raman spectroscopy (SERS),[8,22−25] a variety of nonlinear scattering measurements (hyperRayleigh,[26−28] hyperRaman,[29] and SHG[30]), and time-resolved measurements.[31,32] These techniques are sensitive to the electromagnetic fields at or near the particle surfaces (whereas extinction, at least for small particles, is sensitive to the entire volume of the particle), thus providing important challenges to the development of accurate methods.

This paper begins with a qualitative discussion of the factors that govern plasmon resonance excitation for spherical particles, emphasizing the use of simple electrostatic theories and models. We then give a brief description of modern numerical techniques that can treat arbitrary particles and environments, and then, we describe applications of these techniques to problems of recent interest, particularly to the description of triangular silver particles using a method known as the discrete dipole approximation (DDA). Our applications include studies of the particle size and shape dependence of extinction spectra, the treatment of substrate and solvent effects for nonspherical particles, and the calculation of surface electromagnetic fields. This paper will not consider particle−particle interaction effects, but we should note that several recent studies related to this topic[33−35] use methods related to those discussed here. We
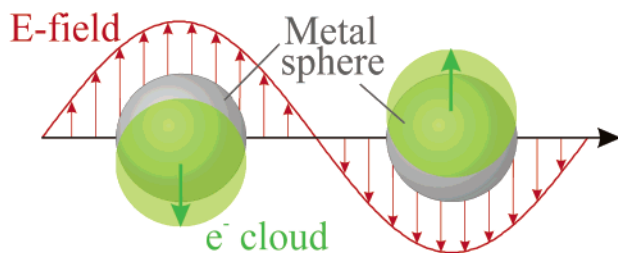
Figure 1. Schematic of plasmon oscillation for a sphere, showing the displacement of the conduction electron charge cloud relative to the nuclei.

should also note that several books and reviews have been published recently on subjects closely related to those considered in this paper.[5]

II. Plasmon Resonances for Small Spherical Particles

A. Dipole Plasmon Resonances. When a small spherical metallic nanoparticle is irradiated by light, the oscillating electric field causes the conduction electrons to oscillate coherently. This is schematically pictured in Figure 1. When the electron cloud is displaced relative to the nuclei, a restoring force arises from Coulomb attraction between electrons and nuclei that results in oscillation of the electron cloud relative to the nuclear framework. The oscillation frequency is determined by four factors: the density of electrons, the effective electron mass, and the shape and size of the charge distribution. The collective oscillation of the electrons is called the dipole plasmon resonance of the particle (sometimes denoted "dipole particle plasmon resonance" to distinguish from plasmon excitation that can occur in bulk metal or metal surfaces). Higher modes of plasmon excitation can occur, such as the quadrupole mode where half of the electron cloud moves parallel to the applied field and half moves antiparallel. For a metal like silver, the plasmon frequency is also influenced by other electrons such as those in d-orbitals, and this prevents the plasmon frequency from being easily calculated using electronic structure calculations. However, it is not hard to relate the plasmon frequency to the metal dielectric constant, which is a property that can be measured as a function of wavelength for bulk metal.

To relate the dipole plasmon frequency of a metal nanoparticle to the dielectric constant, we consider the interaction of light with a spherical particle that is much smaller than the wavelength of light. Under these circumstances, the electric field of the light can be taken to be constant, and the interaction is governed by electrostatics rather than electrodynamics. This is often called the quasistatic approximation, as we use the wavelength-dependent dielectric constant of the metal particle, ϵ_i, and of the surrounding medium, ϵ_o, in what is otherwise an electrostatic theory.

Let's denote the electric field of the incident electromagnetic wave by the vector $\mathbf{E}_o$. We take this constant vector to be in the x direction so that $\mathbf{E}_o = E_o\hat{x}$, where $\hat{x}$ is a unit vector. To determine the electromagnetic field surrounding the particle, we solve LaPlace's equation (the fundamental equation of electrostatics), $\nabla^2\varphi = 0$, where φ is the electric potential and the field $\mathbf{E}$ is related to φ by $\mathbf{E} = -\nabla\varphi$. In developing this solution, we apply two boundary conditions: (i) that φ is continuous at the sphere surface and (ii) that the normal component of the electric displacement $\mathbf{D}$ is also continuous, where $\mathbf{D} = \epsilon\mathbf{E}$.

It is not difficult to show that the general solution to the LaPlace equation has angular solutions which are just the spherical harmonics. In addition, the radial solutions are of the

form r^ℓ and $r^{-(\ell+1)}$, where ℓ is the familiar angular momentum label ($\ell = 0, 1, 2, ...$) of atomic orbitals. If we restrict our considerations for now to just the $\ell = 1$ solution and if $\mathbf{E}_o$ is in the x direction, the potential is simply $\varphi = $ A r $\sin\theta \cos\phi$ inside the sphere ($r < a$) and $\varphi = (-E_o r + B/r^2) \sin\theta \cos\phi$ outside the sphere ($r > a$), where A and B are constants to be determined. If these solutions are inserted into the boundary conditions and the resulting φ is used to determine the field outside the sphere, $\mathbf{E}_{out}$, we get

$$\mathbf{E}_{out} = E_o\hat{x} - \alpha E_o\left[\frac{\hat{x}}{r^3} - \frac{3x}{r^5}(x\hat{x} + y\hat{y} + z\hat{z})\right] \quad (1)$$

where α is the sphere polarizability and $\hat{x}$, $\hat{y}$, and $\hat{z}$ are the usual unit vectors. We note that the first term in eq 1 is the applied field and the second is the induced dipole field (induced dipole moment $= \alpha E_o$) that results from polarization of the conduction electron density.

For a sphere with the dielectric constants indicated above, the LaPlace equation solution shows that the polarizability is

$$\alpha = g_d a^3 \quad (2)$$

with

$$g_d = \frac{\epsilon_i - \epsilon_o}{\epsilon_i + 2\epsilon_o} \quad (3)$$

Although the dipole field in eq 1 is that for a static dipole, the more complete Maxwell equation solution shows that this is actually a radiating dipole, and thus, it contributes to extinction and Rayleigh scattering by the sphere. This leads to extinction and scattering efficiencies given by

$$Q_{ext} = 4x\text{Im}(g_d) \quad (4)$$

$$Q_{sca} = \frac{8}{3}x^4|g_d|^2 \quad (5)$$

where $x = 2\pi a(\epsilon_o)^{1/2}/\lambda$. The efficiency is the ratio of the cross-section to the geometrical cross-section πa^2. Note that the factor g_d from eq 3 plays the key role in determining the wavelength dependence of these cross-sections, as the metal dielectric constant ϵ_i is strongly dependent on wavelength.

B. Quadrupole Plasmon Resonances. For larger particles, higher multipoles, especially the quadrupole term ($\ell = 2$) become important to the extinction and scattering spectra. Using the same notation as above and including the $\ell = 2$ term in the LaPlace equation solution, the resulting field outside the sphere, $\mathbf{E}_{out}$, now can be expressed as

$$\mathbf{E}_{out} = E_o\hat{x} + ikE_o(x\hat{x} + z\hat{z}) - \alpha E_o\left[\frac{\hat{x}}{r^3} - \frac{3x}{r^5}(x\hat{x} + y\hat{y} + z\hat{z})\right] - \beta E_o\left[\frac{x\hat{x} + z\hat{z}}{r^5} - \frac{5z}{r^7}(x^2\hat{x} + y^2\hat{y} + xz\hat{z})\right] \quad (6)$$
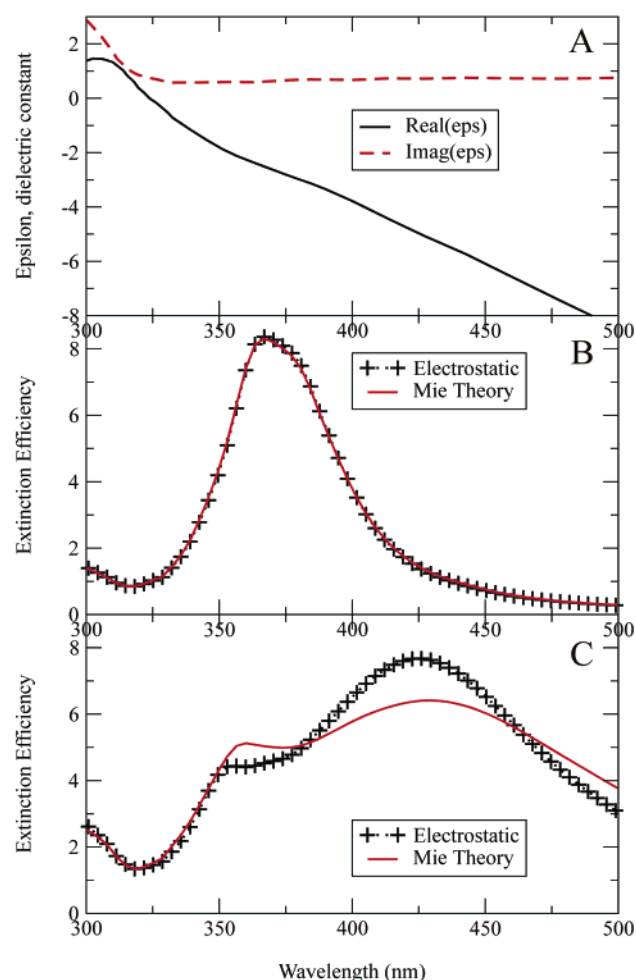
and the quadrupole polarizability is

$$\beta = g_q a^5 \quad (7)$$

with

$$g_q = \frac{\epsilon_i - \epsilon_o}{\epsilon_i + 3/2\epsilon_o} \quad (8)$$

Note that the denominator of eq 8 contains the factor 3/2 while

Figure 2. (a) Real and imaginary part of silver dielectric constants as function of wavelength. Data are from Lynch and Hunter[36] but with a smoothing applied as described in ref 15. (b) Extinction efficiency, i.e., the ratio of the extinction cross-section to the area of the sphere, as obtained from quasistatic theory for a silver sphere whose radius is 30 nm. (c) The corresponding efficiency for a 60 nm particle, including for quadrupole effects, and correcting for finite wavelength effects. In b and c, the exact Mie theory result is also plotted.

in eq 3 the corresponding number is 2. These factors arise from the exponents in the radial solutions to LaPlace's equation, e.g., the factors r^{ℓ} and $r^{-(\ell+1)}$ that were discussed above. For dipole excitation, we have $\ell = 1$, and the magnitude of the ratio of the exponents is $(\ell + 1)/\ell = 2$, while for quadrupole excitation $(\ell + 1)/\ell = 3/2$. Higher partial waves work analogously.

Following the same derivation, we get the following quasistatic (dipole + quadrupole) expressions for the extinction and Rayleigh scattering efficiencies:

$$Q_{ext} = 4x\text{Im}\left[g_d + \frac{x^2}{12}g_q + \frac{x^2}{30}(\epsilon_i - 1)\right] \quad (9)$$

$$Q_{sca} = \frac{8}{3}x^4\left\{\left|g_d\right|^2 + \frac{x^4}{240}\left|g_q\right|^2 + \frac{x^4}{900}\left|\epsilon_i - 1\right|^2\right\} \quad (10)$$

C. Extinction for Silver Spheres. We now evaluate the extinction cross-section using the quasistatic expressions, eqs 4, 5 and 9, 10, as well as the exact (Mie) theory. We take dielectric constants for silver[36] that are plotted in Figure 2a and the external dielectric constant is assumed to be 1 (i.e., a particle in a vacuum). The resulting efficiencies for 30 and 60 nm spheres are plotted in Figure 2b,c, respectively.

The cross-section in Figure 2b shows a sharp peak at 367 nm, with a good match between quasistatic and Mie theory. This peak is the dipole surface plasmon resonance, and it occurs when the real part of the denominator in eq 3 vanishes, corresponding to a metal dielectric constant whose real part is -2. For particles that are not in a vacuum, the plasmon resonance condition becomes $\text{Re } \epsilon_i/\epsilon_o = -2$, and because the real part of the silver dielectric constant decreases with increasing wavelength (Figure 2a), the plasmon resonance wavelength for $\epsilon_o > 1$ is longer than in a vacuum. The plasmon resonance wavelength also gets longer if the particle size is increased above 30 nm. This is due to additional electromagnetic effects that will be discussed later.

Figure 2c presents the $\ell = 2$ quasistatic (dipole + quadrupole) cross-section as well as the full Mie theory result for a radius 60 nm sphere. The quasistatic result also includes a finite wavelength correction that is described further below (Section III.B). We see that the dipole plasmon wavelength has shifted to the red, and there is now a distinct quadrupole resonance peak at 357 nm. This quadrupole peak occurs when the real part of the denominator in eq 8 vanishes, corresponding to a metal dielectric constant whose real part is $-3/2$. For a sphere of this size, there are clear differences between the quasistatic and the Mie theory results; however, the important features are retained. Although Mie theory is not a very expensive calculation, the quasistatic expressions are convenient to use when only qualitative information is needed.

D. Electromagnetic Fields for Spherical Particles. So far, we have emphasized the calculation of extinction and Rayleigh scattering cross-sections; however, for certain properties, such as SERS and hyperRaman scattering (HRS) intensities, it is the electromagnetic field at or near the particle surfaces that determines the measured intensity. Thus, if $\mathbf{E}(\omega)$ is the local field for frequency ω, then the SERS intensity is determined by $\langle|\mathbf{E}(\omega)|^2|\mathbf{E}(\omega')|^2\rangle$ where ω' is the Stokes-shifted frequency and the brackets are used to denote an average over the particle surface. The HRS intensity is similarly (but approximately) determined by $\langle|\mathbf{E}(\omega)|^4|\mathbf{E}(2\omega)|^2\rangle$.[29] Also, when one makes an aggregate or array of metal nanoparticles, the interaction between the particles is determined by the polarization induced in each particle due to the fields $\mathbf{E}$ arising from all of the other particles.

At the dipole (dipole + quadrupole) level, the field outside a particle is given by eq 1 (eq 6). These expressions determine the near-fields at the particle surfaces quite accurately for small enough particles; however, the field beyond 100 nm from the center of the particle exhibits radiative contributions that are not contained in these equations. To describe these, we need to replace the dipole or quadrupole field by its radiative counterpart. In the case of the dipole field, this is given by

$$\mathbf{E}_{dipole} = k^2 e^{ikr}\frac{\mathbf{r} \times (\mathbf{r} \times \mathbf{P})}{r^3} + e^{ikr}(1 - ik\mathbf{r})\frac{[r^2\mathbf{P} - 3\mathbf{r}(\mathbf{r} \cdot \mathbf{P})]}{r^5} \quad (11)$$

where $\mathbf{P}$ is the dipole moment. Note that this reduces to the static field in eq 1 in the limit $k \to 0$ where only the term in square brackets remains. However, at long range, the first term becomes dominant as it falls off more slowly with r than the second.

Figure 3 presents contours of the electric field enhancement $|\mathbf{E}|^2$ around 30 and 60 nm radius silver spheres, based on a Mie theory calculation in which all multipoles are included. Two planes are chosen for these plots, the *xz* plane that is formed by the polarization and k vectors and the *yz* plane that is

Feature Article

*J. Phys. Chem. B, Vol. 107, No. 3, 2003* **671**
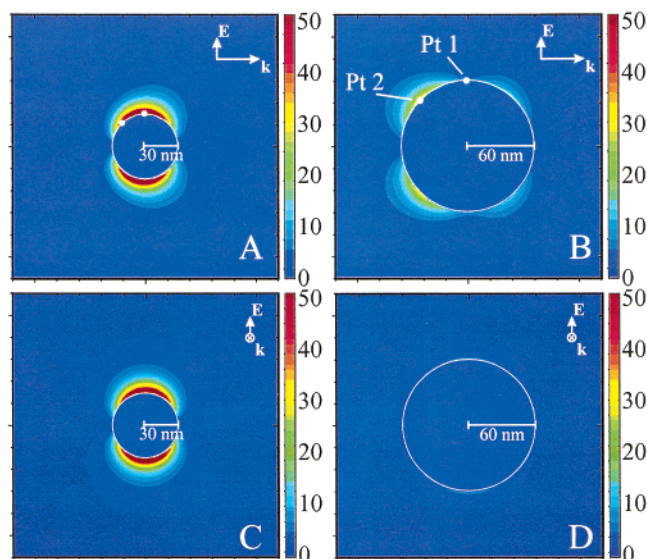
Figure 3. E-field contours for radius 30 and 60 nm Ag spheres in a vacuum. Two cross-sections are depicted for each sphere. (a, b) The plane containing the propagation and polarization axes and (c, d) the plane perpendicular to the propagation axis. The 30 nm sphere refers to 369 nm light, the main extinction peak for this size, whereas the larger sphere is for 358 nm light, the quadrupole peak for this size. Labeled points 1 and 2 illustrate locations for Figure 4.

Figure 4. Comparison of extinction efficiency, surface-averaged E-field enhancement, and E-field enhancement for specific points for radius 30 nm (top) and 60 nm (bottom) Ag spheres in a vacuum. The two points chosen are point 1, along the polarization direction, and point 2, at a 45° angle relative to the polarization direction and in the *xz* plane.

perpendicular to the polarization vector. The wavelength chosen for the 30 nm particle is the dipole plasmon peak, so since the dipole field dominates, we see the characteristic p-orbital shape around the sphere in Figure 3a,c. Note that a small quadupole component to the field makes the p-orbital lobes slightly asymmetrical. At long range, the radiative terms in eq 11 become more important, and then, the field has a characteristic spherical wave appearance.

The wavelength for the 60 nm particle has been chosen to be that for the peak in the quadrupole resonance, and as a result, the field contours close to the particle in Figure 3b look like a d_{xz}-orbital (slightly distorted by a small dipole component that is also present). In addition, Figure 3d, which is a nodal plane for the d_{xz}-orbital, only shows the weak dipolar component. Note that the peak magnitude of the field for the 30 nm particle occurs at the particle surface, along the polarization direction. This peak is over 50 times the size of the applied field, while that for the 60 nm particle is over 25 times larger. This is responsible for the electromagnetic enhancements that are seen in SERS, and they also lead to greatly enhanced HRS.

Figure 4 plots the surface-averaged E-field enhancement for the 30 and 60 nm spheres as a function of wavelength, along with the extinction efficiency. In addition, the figure includes the E-field enhancement associated with two points on the sphere: (a) along the polarization direction (point 1) and (b) rotated 45 degrees away from the polarization direction (point 2). The E-field enhancement associated with specific points on the surface would be appropriate for understanding a single molecule SERS experiment, should this be possible for a spherical particle. For both sphere sizes, the field enhancement due to the dipole resonance peaks to the red of the extinction. Quasistatic theory predicts that both peaks should occur at the same wavelength; however, the finite wavelength corrections to the quasistatic result lead to depolarization of the plasmon excitation on the blue side of the extinction peak, resulting in a smaller average field and a red-shifted peak.

For the smaller sphere (top panel of Figure 4), the E-field enhancement associated with point 1 is about three times larger
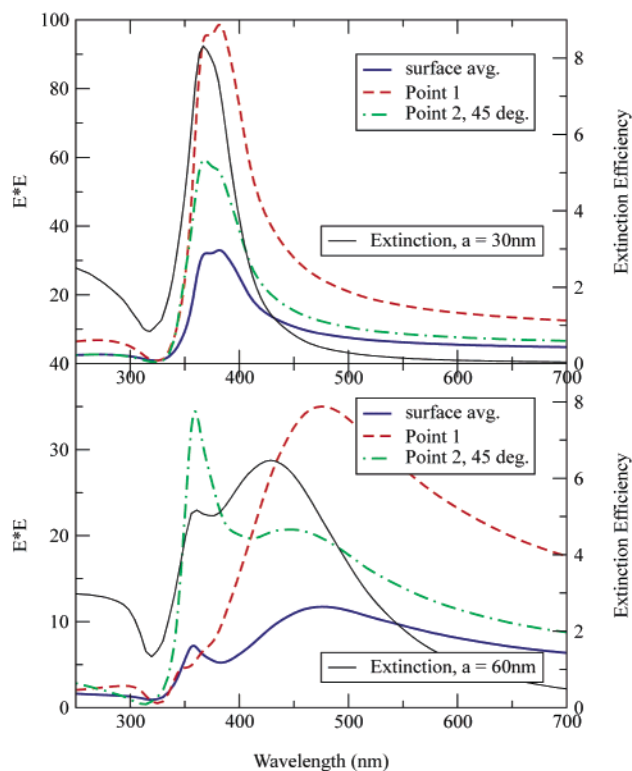
than the surface-averaged value, and the lineshapes are the same. Point 2 shows a smaller enhancement, and it peaks toward the blue, indicating the influence of a weak quadrupole resonance. For the larger sphere (bottom), the maximum for point 1 is about 3.5 times greater than the surface average for the dipole peak. For point 2, we see a maximum at the quadrupole resonance wavelength, and the enhancement is about three times greater than for the quadrupole peak in the surface-averaged result. Thus, for the larger sphere, it is possible for the largest SERS enhancement to be at a location on the surface that is not along the polarization direction.

III. Electrodynamics Methods for Nonspherical Particles

A. Exact Analytical Theories: Spheroids. Mie theory is the exact analytical solution of Maxwell's equations for a sphere. Unfortunately, the only other compact object for which exact solutions are known is a spheroid, and here, the solution is sufficiently complex that little use has been made of the analytical expressions. However, Voshchinnikov and Farafonov (VF)[37] have developed a numerical implementation of the extinction and scattering cross-sections based on this theory, providing a useful tool for understanding a common example of nonspherical nanoparticles.

In Figure 5, we present extinction cross-sections based on the VF code for oblate spheroids having a ratio of major to minor axes, *r*, ranging from *r* = 1 (a sphere) to *r* = 10 (highly oblate). The dimensions of each spheroid have been chosen so that the total volume of each spheroid is equal to that for a 80 nm radius sphere. The field polarization has been chosen to be along the major axis of the spheroid.

Figure 5 shows two important effects. First, as the ratio increases, the dipole plasmon resonance gradually red shifts.
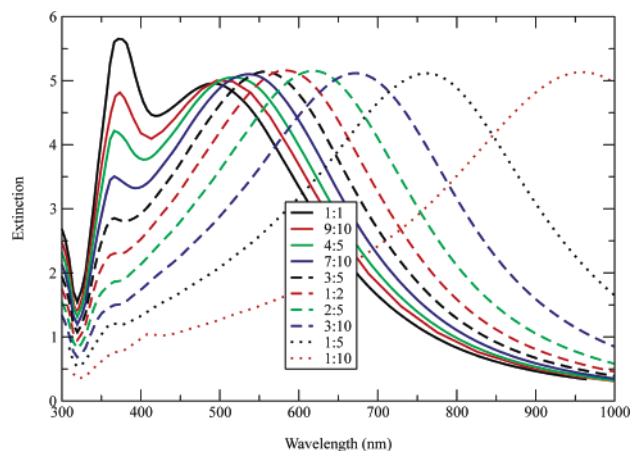
Figure 5. Exact electrodynamic calculation of the extinction spectra of oblate spheroids, all with the same equivalent volume, corresponding to a sphere radius of 80 nm. The major to minor axis ratio, *r*, is from left to right: 10, 5, 3.33, 2.5, 2, 1.67, 1.43, 1.25, 1.11, and 1. In this figure the extinction is normalized to the area of a circle with radius equal to the semi-major axis.

This shows that the plasmon resonance depends strongly on particle shape, shifting to the red as the particle becomes more oblate. There is a second resonance (not plotted) that arises when the polarization is chosen to be along the minor axis, which blue shifts as the particle becomes more oblate. If the spheroid is prolate instead of oblate, there are also two distinct resonances, with the red-shifting one still being associated with the major axis. If the particle is an ellipsoid, with three distinct axes, there are three plasmon resonances.

The second effect seen in Figure 5 is that the quadrupole resonance peak, which for the case of a sphere is larger than the dipole peak, is much less important as *r* is increased. This shows that the quadrupole mode can be "quenched" by particle asymmetry. A consequence of this is that quasistatic theory, which only describes dipole plasmon resonances, is very useful for highly spheroidal large particles, even when this theory fails for spheres.

B. Modified Long Wavelength Approximation (MLWA): Spheroids. The quasistatic approximation was introduced in Section II.A, where we solved the electrostatics associated with light interacting with the particle and simply used the wavelength-dependent dielectric constant in the result. This treatment can easily be generalized to treat spheroids, as described in several papers,[38,39] and it leads to relatively simple expressions for cross-sections and field enhancements. In addition, it can be used for other particle shapes. However, to develop an accurate theory, it is necessary to correct the quasistatic result for finite wavelength effects, leading to what is sometimes called the MLWA.[40]

In the quasistatic treatment, one finds that the induced dipole moment **P** in an oblate spheroid resulting from the imposition of a field **E** is given by

$$\mathbf{P} = \alpha \mathbf{E} \qquad (12)$$

where α is the spheroid polarizability.

$$\alpha = \frac{\epsilon_i - \epsilon_o}{\epsilon_i + \chi \epsilon_o} \frac{b^3 (1+\chi) \xi_o^2 + 1}{3 \qquad \xi_o^2} \qquad (13)$$

and χ and ξ_o are parameters that depend on the geometry of the spheroid:

$$\chi = -1 - 2 \left[\xi_o^2 - \frac{\xi_o(\xi_o^2 + 1)}{2} \cos^{-1}\left(\frac{\xi_o^2 - 1}{\xi_o^2 + 1} \right) \right]^{-1} \qquad (14)$$

$$\xi_o = (b^2/a^2 - 1)^{-1/2} \qquad (15)$$

with *a* and *b* being the minor and major axes, respectively.

Note that the polarizability contains the denominator ($\epsilon_i + \chi \epsilon_o$). This is the same form as we discussed earlier for a sphere (eq 3) except that 2 is replaced by χ. It is easy to show that χ increases with increasing *b/a*, leading to a plasmon resonance that red shifts as the spheroid becomes more oblate. Of course, this is just the result we've already seen in Figure 5.

The electrodynamic corrections associated with MLWA are now introduced by rewriting eq 12 as[41]

$$\mathbf{P} = \alpha[\mathbf{E} + \mathbf{E}_{rad}] \qquad (16)$$

where the radiative correction field $\mathbf{E}_{rad}$ is

$$\mathbf{E}_{rad} = \frac{2}{3} i k^3 \mathbf{P} + \frac{k^2}{b} \mathbf{P} \qquad (17)$$

The first term in eq 17 describes radiative damping. It arises from spontaneous emission of radiation by the induced dipole. This emission grows rapidly with particle size, eventually reducing the size of the induced dipole and increasing the plasmon linewidth. The second term comes from depolarization of the radiation across the particle surface due to the finite ratio of particle size to wavelength. This dynamic depolarization term causes red shifting of the plasmon resonance as the particle size is increased.

The net effect of both of these terms is to produce a modified expression for the dipole moment **P** in which eq 12 is multiplied by the expression

$$F = \left(1 - \frac{2}{3} i k^3 \alpha - \frac{k^2}{b} \alpha \right)^{-1} \qquad (18)$$

Conversion of the dipole moment into an extinction cross-section is similar to the sphere derivation (eq 4) given above, but now, the factor *F* must be carried through. Note that the radiative damping contribution to *F* is proportional to the product of the polarizability (proportional to particle volume) times k³ (= (2π/λ)³). The dynamic depolarization term is proportional to α/b (proportional to particle area) times k². Clearly, both terms will be of order unity when the particle radius becomes comparable to λ/2π, which for λ = 600 nm implies that *b* = 100 nm.

Figure 6 presents a test of the MLWA for oblate spheroids whose equivalent volume is the same as for a sphere of radius 30 nm. The ratio of major to minor axis is chosen to vary from 1 to 10, and both MLWA and exact cross-sections are included. The results show excellent agreement between exact and MLWA for all shapes considered, which indicates that the MLWA gives an accurate description of the full electrodynamics. Again, we see the red shifting of the plasmon resonance as the spheroid becomes more oblate. Quadrupole resonance effects are not important for these 30 nm spheroids, and MLWA would not describe them if they were. However, even for large particles such as those pictured in Figure 5, the MLWA provides an accurate description of everything except the quadrupole contribution.

C. DDA Method. For particles that do not allow solving Maxwell's equations (or LaPlace's equation) analytically, it is necessary to introduce numerical methods. Over the last 15 years, a number of numerical methods have been introduced,

Feature Article

J. Phys. Chem. B, Vol. 107, No. 3, 2003 **673**
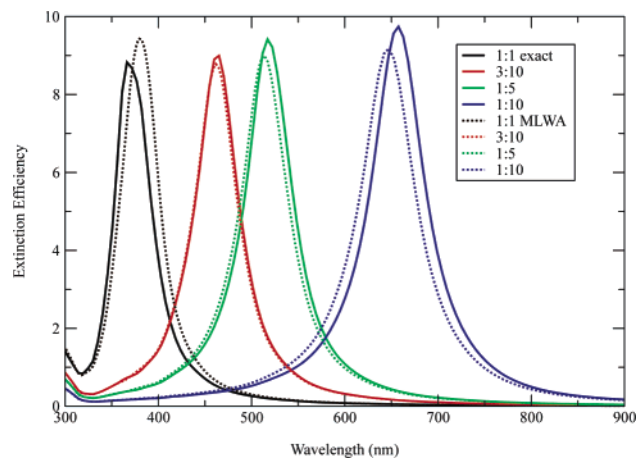
Figure 6. Extinction spectra of oblate silver spheroids, all with the same equivalent volume corresponding to a sphere of $R = 30$ nm. The ratio of major to minor axes is, from left to right, $r = 1$, 3.33, 5, and 10. For each ratio, results are presented using MLWA and the exact solution of Maxwell equations, as indicated in the legend.

Figure 7. E-field enhancement contours external to a 5:1 ellipsoid in a vacuum based on DDA calculations at 775 nm. The ellipsoid's volume is equivalent to a radius 80 nm sphere, and the fields inside the particle are set to zero for clarity. Planes plotted pass through the center of the sphere, with (a) plane chosen perpendicular to the **k** direction, with **E** along the abscissa and (b) plane chosen to contain **k** and **E**, with **k** being the abscissa.

including the DDA,[40,42,43] the multiple mutipole method,[44] and the finite difference time domain method.[45,46] Each of these has particular advantages and disadvantages, but for isolated nanoparticles of arbitrary shape and a complex surrounding environment, a particularly powerful method is the DDA.[15−20] In the following paragraphs, we briefly describe this method.

The DDA method is a numerical method in which the object of interest is represented as a cubic lattice of N polarizable points.[42] There is no restriction as to which of the cubic lattice sites are occupied, which means that DDA can represent an object or multiple objects of arbitrary shape and composition. We take the ith element to have a dipole polarizability α_i (and no higher multipole polarizabilities), with its center at a position denoted $\mathbf{r}_i$. The polarization induced in each element as a result of interaction with a local electric field $\mathbf{E}_{loc}$ is (omitting the frequency factors $e^{i\omega t}$)

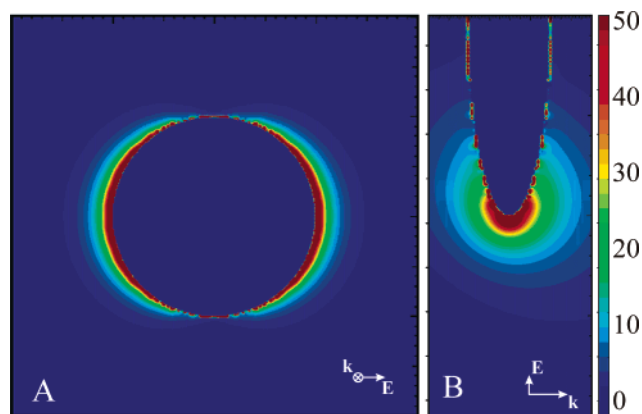$$\mathbf{P_i} = \alpha_i \cdot \mathbf{E}_{loc}(\mathbf{r_i}) \tag{19}$$

$\mathbf{E}_{loc}$, for isolated particles, is the sum of an incident field and a contribution from all other dipoles in the particle

$$\mathbf{E}_{loc}(\mathbf{r_i}) = \mathbf{E}_{loc,i} = \mathbf{E}_{inc,i} + \mathbf{E}_{dipole,i} =$$
$$\mathbf{E_o} \exp(i\mathbf{k} \cdot \mathbf{r_i}) - \sum_{j \neq i} \mathbf{A}_{i,j} \cdot \mathbf{P_j} \tag{20}$$

$\mathbf{E_o}$ and $\mathbf{k}$ are the amplitude and wave vector of the incident wave, respectively, and the interaction matrix $\mathbf{A}$ has the following form (for $j \neq i$)

$$\mathbf{A}_{ij} \cdot \mathbf{P_j} = \frac{\exp(ik\mathbf{r}_{ij})}{\mathbf{r}_{ij}^3} \times$$
$$\left\{ k^2 \mathbf{r}_{ij} \times (\mathbf{r}_{ij} \times \mathbf{P_j}) + \frac{(1 - ik\mathbf{r}_{ij})}{\mathbf{r}_{ij}^2} [\mathbf{r}_{ij}^2 \mathbf{P_j} - 3\mathbf{r}_{ij}(\mathbf{r}_{ij} \cdot \mathbf{P_j})] \right\} \tag{21}$$

where $k = \omega/c$. Note that the metal dielectric constant and that of the surroundings enter into the calculation through a factor ϵ_i/ϵ_o, which is contained in the polarizabilities α_i. In addition, the wavevector k should be multiplied by $(\epsilon_o)^{1/2}$ if the particle is not in vacuum. The explicit formula for α_i was developed by Draine and Goodman[43] such that the dipole lattice for an infinite solid exactly reproduces the continuum dielectric response of

that solid to electromagnetic radiation. This leads to a theory that is not exact, but in practice, it gives extinction spectra for metal particles that are within 10% of the exact results, and this agreement appears to be independent of the size, shape, or composition of the particle.

Substituting eqs 20 and 21 into eq 19 and rearranging terms in the equation, we generate an equation of the form

$$\mathbf{A}' \cdot \mathbf{P} = \mathbf{E} \tag{22}$$

where $\mathbf{A}'$ is a matrix, which is built out of the matrix $\mathbf{A}$ from eq 20. For a system with a total of N elements, $\mathbf{E}$ and $\mathbf{P}$ in eq 22 are 3N-dimensional vectors, and $\mathbf{A}'$ is a 3N × 3N matrix. By solving these 3N complex linear equations, the polarization vector $\mathbf{P}$ is obtained, and with this, the extinction cross-sections and other optical properties may be calculated. In actual practice, there are significant advantages associated with performing the sum over dipole fields in eq 20 using fast Fourier transform methods and solving eq 22 by complex conjugate gradient techniques. This is the implementation developed in the work of Draine and Flatau,[43] and it is what we have used in the present studies. Further details of the method are described in ref 40.

As an example of the use of DDA calculations, in Figure 7, we present electric field contours for a 5:1 oblate spheroidal silver particle (whose volume is equivalent to a sphere of radius 80 nm) at a wavelength, 775 nm, that corresponds to the plasmon maximum. In earlier work, we demonstrated that this calculation gives cross-sections in nearly quantitative agreement with MLWA results.[20] The gridding associated with the DDA calculation is evident in the somewhat distorted appearance of the particle surfaces, but we see that except for the layer closest to the surface, the fields are smooth and well-converged. The plot shows that the field contours are much more intense near the particle surfaces than was the case for the sphere contours presented in Figure 3, with the peak field being 140 times the applied field. This is why SERS intensities are much higher for more oblate (or prolate) particles. Some of this arises because the fields near a curved surface are intrinsically higher for higher curvatures. (This is sometimes called the lightning rod effect.) In addition, the red-shifted plasmon (as compared to a sphere) can have a narrower plasmon resonance due to decreased importance of interband transitions (an effect that is important to the imaginary part of the metal dielectric constant).
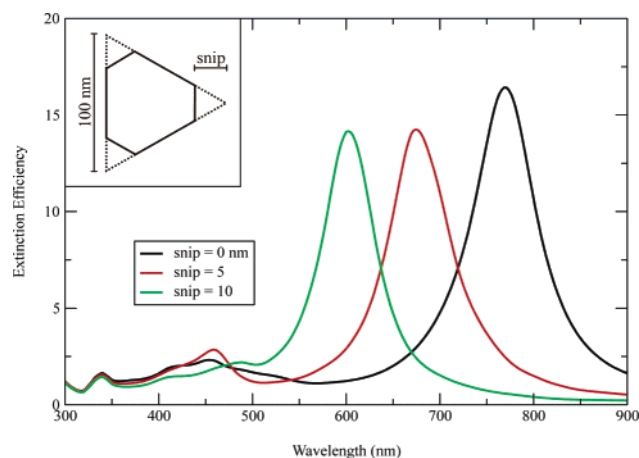
Figure 8. Orientation-averaged extinction efficiency for trigonal prisms based on a 100 nm edge dimension with snips of 0, 10, and 20 nm. The inset shows the shape of a snipped prism. The prism thickness is 16 nm. Results are based on DDA calculations with a 2 nm cubic grid. For snip = 0, 68 704 dipoles are used in the calculation.

IV. Applications

In this section, we present applications in which the DDA method has been used to describe nonspherical silver nanoparticles. In part A, we describe studies of triangular nanoprisms that have recently been made using wet chemistry methods, while in part B, we consider lithographically fabricated truncated tetrahedrons in complex dielectric environments. Both types of particles are being used for chemical and biological sensing applications,[6,8,18,19] but they may find many other applications due to their highly controllable optical properties.

A. Triangular Prisms in Solution. An important recent discovery[13] in the field of colloid chemistry is that it is possible to use wet chemistry methods to make triangular prisms of silver that have atomically flat surfaces and do not aggregate. However, the distribution of sizes and shapes generated so far is relatively broad, with many of the particles having missing tips. To model these spectra, we have done DDA calculations for both perfect triangular prisms and for "snipped" prisms, in which the ends of all three tips have been removed. All calculations refer to water as the external dielectric medium. Figure 8 presents the resulting spectra, with the insert to Figure 8 showing the geometry of a snipped prism. The perfect triangles are 100 nm in edge length and 16 nm thick, which is typical of what has been produced in experiment. The DDA calculations use a cubic grid that is 2 nm in each dimension. This leads to extinction spectra that are converged with respect to grid size. All of the results in Figure 8 refer to an average over polarization directions. We have compared full angular averaging with averaging over the three Cartesian directions, and we find that the latter procedure is sufficient to mimic a fully averaged result. Later, we will examine results for specific polarizations.

The results in Figure 8 show spectra, which for the most part consist of three peaks, a long wavelength peak at 770 nm (here referring to the perfect triangle), a weaker peak at 460 nm, and a small but sharp peak at 335 nm. In addition, we see that the red-most peak is very sensitive to snipping, with the 20 nm snipped prism giving a peak that is blue-shifted by 100 nm as compared to the perfect prism. The other peaks are more weakly sensitive to snipping.

To further understand these spectra, in Figure 9a, we present three calculated spectra for the 10 nm snipped triangle, one for polarization along each principle axis of the prism. All three calculated spectra have two peaks, and the two polarizations
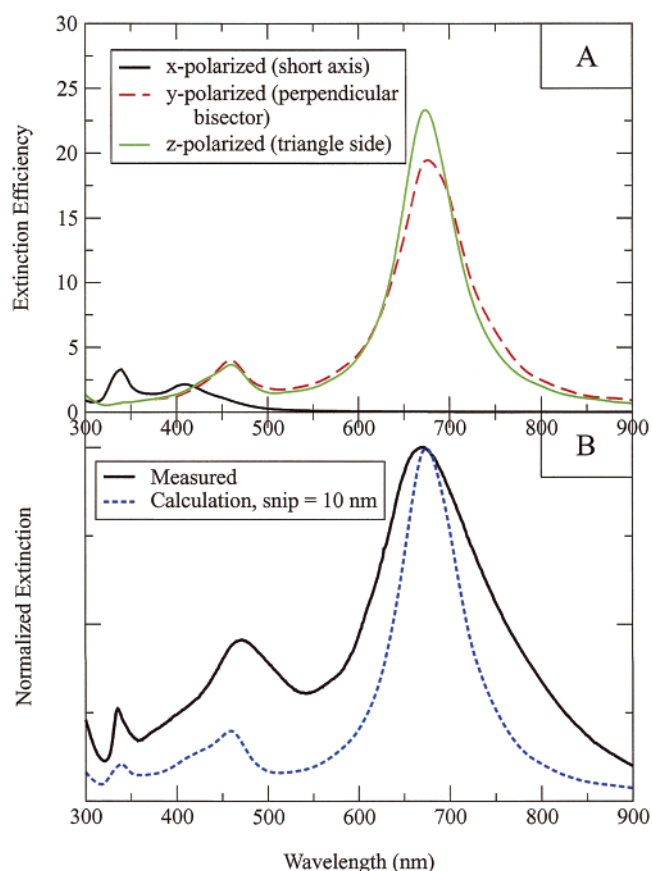

Figure 9. UV−vis spectra of trigonal Ag prisms with side length = 100 nm, snip = 10 nm, and thickness = 16 nm. (a) Calculated spectra for polarization along the three primary symmetry axes. (b) Average over orientation, along with measured spectrum.

along the long axes of the prism (side and perpendicular bisector) closely resemble each other. Thus, the polarization-resolved spectra show peaks at 460 and 670 nm (for in-plane polarization) and 335 and 430 nm (for out-of-plane polarization). In Figure 9b, we show the comparison of orientation-averaged spectra with experiment. The agreement is excellent, confirming that the 10 nm snipped structure (shown in the inset) provides a good representation of the average over particle shapes and sizes. Note that although there are four peaks in the polarization-resolved spectra, the peak at 430 has washed out of the polarization-averaged spectra.

To assign the resonances in Figure 9, plots of the induced polarization were made for each of the resonance wavelengths, for an unsnipped prism. (The results are analogous for a snipped prism.) Figure 10 presents the plots for the 460 and 770 nm peaks. For the 770 nm result, the response appears analogous to the dipole resonance of spheres (such as in Figure 3), with the largest induced polarization and the largest field ($|\mathbf{E}|^2$ over 500 times the applied field) occurring at the particle tips. When excited at 460 nm, the field pattern is much different, with only about half the particle showing significant polarization and very little polarization at the tips. Although hard to see in the figure, dipoles at the rightmost tip point opposite to the incident polarization direction. The pattern closely resembles a quadrupole pattern from electrostatics. From this analysis, we assign the resonances at 770 and 460 nm as dipole and quadrupole plasmon resonances associated with in-plane polarization.

Polarization plots for short axis polarization are more difficult to visualize and interpret. However, it is possible to say that at 430 nm most of the polarization is parallel to the symmetry

Feature Article

J. Phys. Chem. B, Vol. 107, No. 3, 2003 **675**
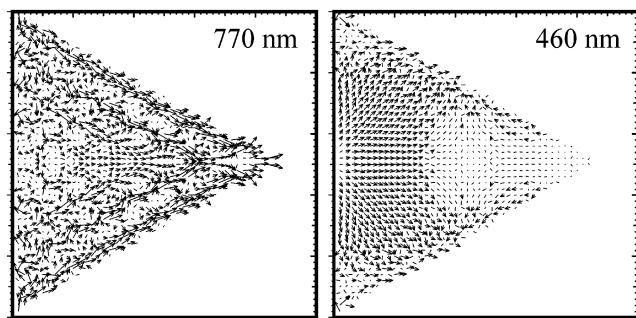
Figure 10. Polarization vectors for dipole (left) and quadrupole (right) resonances at 770 and 460 nm, respectively, for Ag trigonal prisms described in Figure 9.
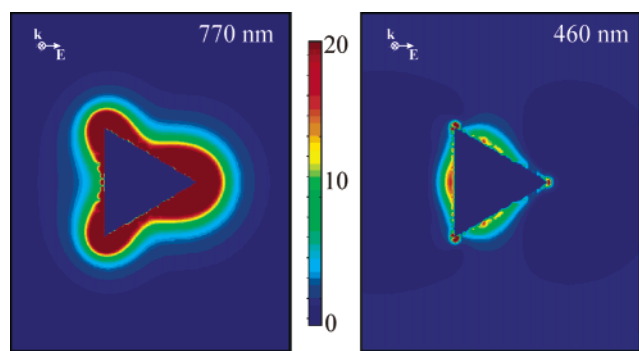
Figure 11. E-field enhancement contours external to the Ag trigonal prism, for a plane that is perpendicular to the trigonal axis and that passes midway through the prism. The light is chosen to have **k** along the trigonal axis and **E** along the abscissa. Left: 770 nm. Right: 460 nm. Side length = 100 nm, and thickness = 16 nm.

axis, as would be the case for a dipole plasmon resonance, while at 335 nm, roughly half the polarization points up and half down, as with a quadrupole resonance. Thus, we find that both in-plane and out-of-plane excitation lead to dipole and quadrupole resonances. All of these features are seen in the experiments except the out-of-plane dipole resonance at 430. Theory indicates that this should be a broad resonance, so it is not surprising that this is not resolved in the measurements. A surprising feature of our results is that the two quadrupole resonances are intense for triangularly shaped particles but not for spheroidal ones of roughly equivalent dimensions.

Figure 11 shows the E-field enhancement contours for a prism with the same orientation as in Figure 10. Here, we see that the maximum enhancement for the dipole resonance is at the tips, while for the quadrupole resonance the significant regions of enhancement occur at the sides. Another important difference, especially at the particle tips, is that the field decays away from the surface faster for the quadrupole than for the dipole.

B. Truncated Tetrahedrons: Effect of Dielectric Environment. *B.1. Solvent Effects.* The effect of the surrounding solvent on the plasmon resonance wavelength of spherical nanoparticles is easily understood using the plasmon resonance condition $\text{Re}(\epsilon_i) + 2\epsilon_o = 0$.

Using the Drude model for the metal dielectric constant, $\epsilon_i = 1 - \omega_{p,b}^2/\omega(\omega + i\gamma)$ where $\omega_{p,b}$ is the bulk plasmon frequency and γ is its width, then it is not difficult to show that as long as $\omega_{p,b} \gg \gamma$, the particle plasmon wavelength λ_p varies with solvent index of refraction $n_o = (\epsilon_o)^{1/2}$ as

$$\lambda_p = \lambda_{p,b}(2n_0^2 + 1)^{1/2} \approx 3^{1/2}\lambda_{p,b}\left\{1 + \frac{1}{3}[n_0 - 1]\right\} \quad (23)$$
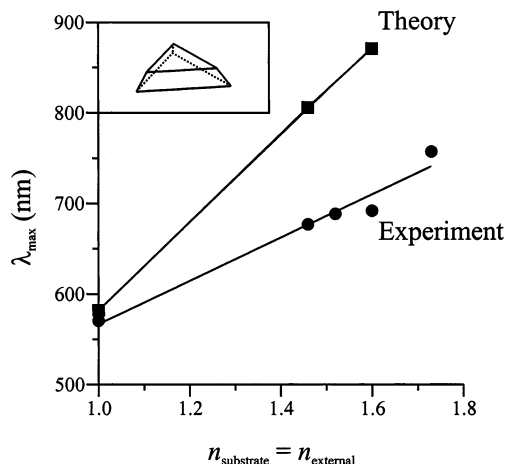
Figure 12. DDA studies of the effect of external dielectric constant on plasmon resonance wavelength for truncated tetrahedral silver particles (structure shown in inset). The experimental data[18] refer to index-matched substrate and solvent, so that the particle can be modeled as having a uniform external dielectric constant.

where $\lambda_{p,b}$ is the bulk plasmon wavelength and we have assumed that $n_o \approx 1$. Equation 23 is only a qualitative theory, but it does reveal that the plasmon wavelength varies roughly linearly with the index of refraction of the surrounding solvent and with a proportionality constant that depends on the plasmon wavelength $3^{1/2}\lambda_{p,b}$ of the particle in a vacuum.

Although eq 23 was derived for spherical particles, a similar proportionality exists for nonspherical particles. Figure 12 shows an example of this for silver-truncated tetrahedrons (whose structure is shown in the inset to the figure). These particles are fabricated by a lithographic technique, so they are produced on a flat surface; however, it is possible to measure plasmon resonance wavelengths using a combination of solvents and surfaces that are indexed matched, in which case the particles may be treated as if they were in a homogeneous solvent. The figure shows the results of DDA calculations, along with experimental results,[18] and we see that both theory and experiment show the linear dependence of plasmon wavelength on index of refraction. Unfortunately, theory and experiment are not in agreement with respect to the slopes of the lines. This is likely due to the presence of an oxide coating on the silver particles, which is unavoidably produced during fabrication, and there may also be chemical interactions between the metal and its surroundings that are left out in the simple dielectric environment model that we have considered. These effects could, in principle, be described by adding a layer around the particle to the DDA calculation; however, the dielectric properties of this layer would need to be determined in order to produce a quantitative theory.

B.2. Substrate Effects. Because nanoparticles are often produced on surfaces, it is important to understand how their interaction with the substrate influences their plasmon resonance properties. This adds a new level of complexity to the electromagnetic modeling due to the asymmetric environment; however, we have found that the DDA method provides a powerful technique, if carefully used, to describe this situation.

To understand the effect of interaction of a particle with a substrate, we have done DDA calculations that model a silver sphere sinking into a substrate. Figure 13 shows the results for a 10 nm sphere engulfed by a mica substrate, including the cases where no mica is present (i.e., a sphere surrounded by vacuum)
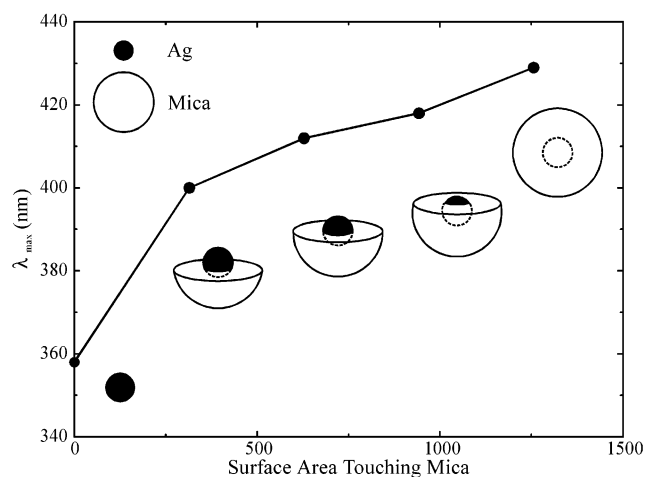
Figure 13. DDA results for a sinking sphere model to investigate shift due to substrate. Peak wavelength vs surface area (in nm²) of radius 10 nm Ag sphere in contact with a partial 10 nm thick mica shell. The metal core is progressively embedded into a partial sphere of mica at 0, 5, 10, and 15 nm from the edge along the core's diameter. A sudden shift occurs between the bare Ag core and shallow immersion, after which the shift is nearly linear with contact area.

and when the Ag core is completely enclosed. We see that the LSPR wavelength shifts dramatically to the red as the sphere goes from free to being partially embedded (25% of the sphere area is exposed). As the sphere becomes increasingly more embedded (area exposed varies from 25 to 100%), the shift to the red is much slower and is approximatelly linear with exposed area.

Figure 14a demonstrates how the influence of the substrate can be essential in obtaining the correct resonance wavelength from a DDA calculation.[17] Here, a truncated tetrahedron with and without an attached slab of mica substrate (see inset) is compared to the measured spectrum. In preparation for this study, a survey of the effect of different slab dimensions was made, and it was found that circular cylindrical slabs with diameters twice the particle width and lengths equal to the particle heights are ideal. Larger slabs do not significantly shift the spectra but require more computational effort. The presence of the substrate slab shifts the extinction peak by about 100 nm to the red, resulting in a peak value that closely matches the measured value. Such an excellent match between measurement and model is not typical, but it is an encouraging example of how attention to details of the experiment leads to a more accurate prediction.

A more detailed study of the effect of substrate index of refraction on the plasmon wavelength associated with truncated tetrahedral particles is presented in Figure 14b, along with comparison with experiment.[18] The figure shows that the substrate-induced spectral shift depends linearly on the refractive index of the substrate slab, with a slope, relative to the slope of Figure 12, that reflects the "exposed area" concept that we discussed in the context of Figure 13. What we mean by this is that the area of the particle exposed to the surface is about one-third of the total particle area, so we expect (and we find) that the slope associated with the substrate is about one-third that associated with the index-matched experiment. This behavior of the relative slopes matches experiment quite well, but the magnitude of both slopes is about twice what is measured in the experiments. We assume that the error in slopes reflects the same issues as were considered in the discussion of Figure 12.
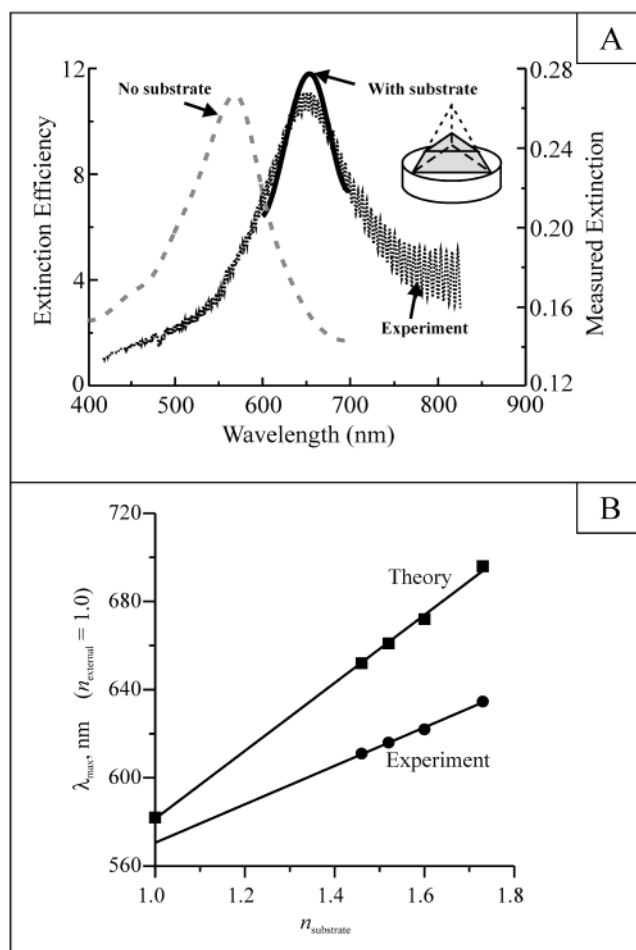
Figure 14. (a) DDA results for the effect of substrate on extinction of a truncated tetrahedron. Comparison with experiment[17] is also included. The particle (see inset) is characterized by a perpendicular bisector = 93 nm, particle height = 28 nm. The DDA calculations include results both with and without a mica slab, where the slab is a cylinder having base diameter = 153 nm and base height = 30 nm. A total of 63 126 dipoles were used to represent the particle + slab, and the results are averaged over the two polarizations that are perpendicular to the three-fold axis. Fringes in the experimental data are due to diffraction with the layered mica substrate. (b) Wavelength associated with plasmon peak associated for a truncated tetrahedral particle as a function of index of refraction of substrate, including comparison of theory and experiment.[18] In this case, the truncated tetrahedron has a perpendicular bisector of 100 nm and a height of 25 nm. The experimental results involve measurements with the following substrates: fused silica, glass, boro-silicate glass, mica, and SF-10 (a specialty, high-index glass). The DDA calculations are based on the same slab model as in (a).

V. Conclusion

The theory and examples presented here indicate that it is now possible to describe many optical properties of silver (and other) metal nanoparticles having complex shapes and which are in complex dielectric environments. The comparisons with experiment show that classical electromagnetic theory works well provided that we have good measurements of particle structure and provided that the complex dielectric environment is properly characterized and modeled. The particles we have considered here are large enough that size dependence of the dielectric constant has not been an issue; however, for smaller particles, this will be an important factor.

This work has emphasized comparisons with experiment for extinction spectra. The calculation of other properties, such as SERS and HRS intensities, provides new challenges for non-spherical particles that are an important component of our

Feature Article

J. Phys. Chem. B, Vol. 107, No. 3, 2003 **677**

current research. We have emphasized in this paper the optical properties of particles that are sufficiently dispersed that they may be treated as being isolated. However, in most practical situations, particle interactions are important, and sometimes they are dominant. Theories for treating such interactions have been described elsewhere;[33,34] however, there is still much to learn about particle interactions.

The survey presented here has emphasized the importance of simple analytical theories for simple shapes, i.e., the MLWA for spheres and spheroids, in providing qualitative insight about the variation of plasmon resonance properties with particle size, shape, and environment. Such quasistatic theories have historically considered only dipole plasmon resonance effects, but here, we have demonstrated that they can be generalized to quadrupole resonances. Although quadrupole resonances are mostly known for spherical and nearly spherical particles, we have demonstrated that they are surprisingly important for triangular prisms.

The workhorse of our studies of nonspherical/nonspheroidal particles is the DDA method. Although other grid-based methods exist, the DDA casts itself very naturally to the treatment of complex particles in heterogeneous environments and to the determination of far-field properties such as extinction and scattering spectra. One of the advantages of the DDA method is that every problem can be approached in the same way, i.e., by defining grids that represent the complex environment and that are sufficiently fine so that converged results are produced. Two weaknesses of the DDA approach are (i) that the total volume of material that can be described is limited by available computer resources to dimensions of a few hundred nanometers and (ii) that the electric fields close to particle surfaces are inaccurate.

References and Notes

(1) Faraday, M. *Philos. Trans.* **1857**, *147*, 145.

(2) Mie, G. *Ann. Phys.* **1908**, *25*, 377.

(3) Kerker, M. *The Scattering of Light and Other Electromagnetic Radiation*; Academic: New York, 1969.

(4) Bohren, C. F.; Huffman, D. R. *Absorption and Scattering of Light by Small Particles*; Wiley Interscience: New York, 1983.

(5) (a) Kreibig, U.; Vollmer, M. *Optical Properties of Metal Clusters*; Springer Series in Materials Science 25; Springer: Berlin, 1995. (b) Kreibig, U. In *Handbook of Optical Properties*; Vol. II: *Optics of Small Particles, Interfaces and Surfaces*; Hummel, R. E., Wissmann, P., Eds.; CRC Press: Boca Raton, 1997; pp 145−190.

(6) (a) Mirkin, C. A.; Letsinger, R. L.; Mucic, R. C.; Storhoff, J. J. *Nature* **1996**, *382*, 607. (b) Elghanian, R.; Storhoff, J. J.; Mucic, R. C.; Letsinger, R. L.; Mirkin, C. A. *Science* **1997**, *277*, 1078.

(7) (a) Quinten, M.; Leitner, A.; Krenn, J. R.; Aussenegg, F. R. *Opt. Lett.* **1998**, *23*, 1331. (b) Brongersma, M. L.; Hartman, J. W.; Atwater, H. A. *Phys. Rev. B* **2000**, *62*, 16356.

(8) (a) Van Duyne, R. P.; Hulteen, J. C.; Treichel, D. A. *J. Chem. Phys.* **1993**, *99*, 2101. (b) Hulteen, J. C.; Van Duyne, R. P. *J. Vac. Sci. Technol.* **1995**, *A13*, 1553.

(9) Kahl, M.; Voges, E.; Hill, W. *Spectrosc. Eur.* **1998**, *10*, 12.

(10) (a) Hornyak, G. L.; Patrissi, C. J.; Martin, C. R.; Valmalette, J. C.; Dutta, J.; Hofmann, H. *Nanostruct. Mater.* **1997**, *9*, 575. (b) Oldenburg, S. J.; Averitt, R. D.; Westcott, S. L.; Halas, N. J. *Chem. Phys. Lett.* **1998**, *288*, 243.

(11) (a) Liao, P. F.; Stem, M. B. *Opt. Lett.* **1982**, 7, 483. (b) Collier, C. P.; Saykally, R. J.; Shiang, J. J.; Henrichs, S. E.; Heath, J. R. *Science* **1997**, *277*, 1978.

(12) (a) Petroski, J. M.; Wang, Z. L.; Green, T. C.; El-Sayed, M. A. *J. Phys. Chem.* **1998**, *B 102*, 3316. (b) Yu, Y. Y.; Chang, S. S.; Lee, C. L.; Wang, C. R. C. *J. Phys. Chem.* **1997**, *B 101*, 6661.

(13) Jin, R.; Cao, Y.; Mirkin, C. A.; Kelly, K. L.; Schatz, G. C.; Zheng, J.-G. *Science* **2001**, *294*, 1901.

(14) Michaels, A. M.; Nirmal, M.; Brus, L. E. *J. Am. Chem. Soc.* **1999**, *121*, 9932.

(15) Jensen, T.; Kelly, L.; Lazarides, A.; Schatz, G. C. *J. Cluster Sci.* **1999**, *10*, 295.

(16) Jensen, T. R.; Schatz, G. C.; Van Duyne, R. P. *J. Phys. Chem.* **1999**, *B103*, 2394.

(17) Jensen, T. R.; Duval, M. L.; Kelly, K. L.; Lazarides, A. A.; Schatz, G. C.; Van Duyne, R. P. *J. Phys. Chem. B* **1999**, *103*, 9846.

(18) Malinsky, M. D.; Kelly, K. L.; Schatz, G. C.; Van Duyne, R. P. *J. Phys. Chem. B* **2001**, *105*, 2343.

(19) Malinsky, M. D.; Kelly, K. L.; Schatz, G. C.; Van Duyne, R. P. *J. Am. Chem. Soc.* **2001**, *123*, 1471.

(20) Kelly, K. L.; Jensen, T. R.; Lazarides, A. A.; Schatz, G. C. In *Metal Nanoparticles: Synthesis, Characterization and Applications*; Feldheim, D., Foss, C., Ed.; Marcel-Dekker: New York, 2002; p 89.

(21) Felidj, N.; Aubard, J.; Levi, G. J. *Chem. Phys.* **1999**, *111*, 1195.

(22) (a) Metiu, H.; Das, P. *Annu. Rev. Phys. Chem.* **1984**, *35*, 507. (b) Metiu, H. *Prog. Surf. Sci.* **1984**, *17*, 153. (c) Adrian, F. *Chem. Phys. Lett.* **1981**, *78*, 45. (d) Wang, D. S.; Kerker, M. *Phys. Rev.* **1981**, *B 24*, 1777. (e) Gersten, J.; Nitzan, A. J. *Chem. Phys.* **1980**, *73*, 3023.

(23) Schatz, G. C. *Acc. Chem. Res.* **1984**, *17*, 370.

(24) Kerker, M. *Acc. Chem. Res.* **1984**, *17*, 271.

(25) Moskovits, M. *Rev. Mod. Phys.* **1985**, *57*, 783.

(26) Dadap, J. I.; Shan, J.; Eisenthal, K. B.; Heinz, T. F. *Phys. Rev. Lett.* **1999**, *83*, 4045.

(27) Johnson, R. C.; Li, J.-T.; Hupp, J. T.; Schatz, G. C. *Chem. Phys. Lett.* **2002**, *356*, 534.

(28) Novak, J. P.; Brousseau, L. C., III; Vance, F. W.; Johnson, R. C.; Lemon, B. I.; Hupp, J. T.; Feldheim, D. L. *J. Am. Chem. Soc.* **2000**, *122*, 12029.

(29) Yang, W. H.; Hulteen, J.; Schatz, G. C.; Van Duyne, R. *J. Chem. Phys.* **1996**, *104*, 4313.

(30) (a) Chen, C. K.; de Castro, A. R. B.; Shen, Y. R. *Phys. Rev. Lett.* **1981**, *46*, 145. (b) Boyd, C. T.; Rasing, T.; Leite, J. R. R.; Shen, Y. R. *Phys. Rev.* **1984**, *B30*, 519−526.

(31) Hartland, G. V. J. *Chem. Phys.* **2002**, *116*, 8048.

(32) Link, S.; El-Sayed, M. A.; Schaaf, G. T.; Whetten, R. L. *Chem. Phys. Lett.* **2002**, *356*, 246.

(33) Lazarides, A. A.; Schatz, G. C. *J. Phys. Chem. B* **2000**, *104*, 460.

(34) Lazarides, A. A.; Schatz, G. C. *J. Chem. Phys.* **2000**, *112*, 2987.

(35) (a) Markel, V. A.; Shalaev, V. M.; Zhang, P.; Huynh, W.; Tay, L.; Haslett, T. L.; Moskovits, M.. *Phys. Rev. B* **1999**, *59*, 10903. (b) Vlckova, B.; Douketis, C.; Moskovits, M.; Shalaev, V. M.; Markel, V. A. *J. Chem. Phys.* **1999**, *110*, 8080.

(36) Lynch, D. W.; Hunter, W. R. In *Handbook of Optical Constants of Solids*; Palik, E. D., Ed.; New York: Academic Press: 1985; pp 350−356.

(37) Voshchinnikov, N. V.; Farafonov, V. G. Optical properties of spheroidal particles. *Astrophys. Space Sci.* **1993**, *204*, 19.

(38) Zeman, E. J.; Schatz, G. C. In *Dynamics of Surfaces, Proceedings of the 17th Jerusalem Symposium*; Pullman, B., Jortner, J., Gerber, B., Nitzan, A., Eds.; Reidel: Dordrecht, 1984; p 413.

(39) Zeman, E. J.; Schatz, G. C. *J. Phys. Chem.* **1987**, *91*, 634.

(40) Yang, W. H.; Schatz, G. C.; Van Duyne, R. P. *J. Chem. Phys.* **1995**, *103*, 869.

(41) (a) Meier, M.; Wokaun, A. *Opt. Lett.* **1983**, *8*, 581. (b) Wokaun, A.; Gordon, J. P.; Liao, P. F. *Phys. Rev. Lett.* **1982**, *48*, 957.

(42) Purcell, E. M.; Pennypacker, C. R. *Astrophys. J.* **1973**, *186*, 705.

(43) (a) Draine, B. T.; Flatau, P. J. *J. Opt. Soc. Am. A* **1994**, *11*, 1491. (b) Draine, B. T.; Goodman, J. J. *Astrophys. J.* **1993**, *405*, 685. (c) Draine, B. T.; Flatau, P. J. *Program DDSCAT*; Scripps Institute of Oceanography, University of California: San Diego, CA.

(44) Moreno, E.; Erni, D.; Hafner, C. Vahldieck, R. *J. Opt. Soc. A* **2002**, *19*, 101.

(45) (a) Novotny, L.; Pohl, D. W.; Hecht, B. *Opt. Lett.* **1995**, *20*, 970. (b) Novotny, L.; Bian, R. X.; Xie, X. S. *Phys. Rev. Lett.* **1997**, *79*, 645.

(46) (a) Bian, R. X.; Dunn, R. C.; Xie, X.; Leung, P. T. *Phys. Rev. Lett.* **1995**, *75*, 4772. (b) Taflove, A. *Computational Electrodynamics: The Finite-Difference Time-Domain Method*; Artech House: Boston, 1995; pp 599.